

Chandra Observations of low velocity dispersion groups

Stephen F. Helsdon¹

*The Observatories of the Carnegie Institute of Washington, 813 Santa Barbara Street,
Pasadena, CA 91101, USA*

and

*School of Physics and Astronomy, University of Birmingham, Edgbaston, Birmingham B15
2TT, UK*

Trevor J. Ponman

*School of Physics and Astronomy, University of Birmingham, Edgbaston, Birmingham B15
2TT, UK*

and

J. S. Mulchaey

*The Observatories of the Carnegie Institute of Washington, 813 Santa Barbara Street,
Pasadena, CA 91101, USA*

ABSTRACT

Deviations of galaxy groups from cluster scaling relations can be understood in terms of an excess of entropy in groups. The main effect of this excess is to reduce the density and thus luminosity of the intragroup gas. Given this, groups should also show a steep relationship between X-ray luminosity and velocity dispersion. However, previous work suggests that this is not the case, with many measuring slopes flatter than the cluster relation.

Examining the group $L_X : \sigma$ relation shows that much of the flattening is caused by a small subset of groups which show very high X-ray luminosities for their velocity dispersions (or vice versa).

Detailed Chandra study of two such groups shows that earlier ROSAT results were subject to significant ($\sim 30\text{-}40\%$) point source contamination, but confirm that a significant hot IGM is present in these groups, although these are two of the coolest systems in which intergalactic X-ray emission has been detected.

¹sfh@star.sr.bham.ac.uk

Their X-ray properties are shown to be broadly consistent with those of other galaxy groups, although the gas entropy in NGC 1587 is unusually low, and its X-ray luminosity correspondingly high for its temperature, compared to most groups.

This leads us to suggest that the velocity dispersion in these systems has been reduced in some way, and we consider how this might have come about.

Subject headings: X-rays: galaxies: clusters – X-rays: galaxies – intergalactic medium – galaxies: clusters: general – galaxies: evolution

1. Introduction

Detailed X-ray studies of the hot intergalactic medium (IGM) in groups became possible for the first time with ROSAT (Mulchaey et al. 1996; Ponman et al. 1996), allowing the basic properties of the IGM in groups to be established and compared to that in rich clusters. Groups are found to depart systematically from cluster trends, showing lower X-ray luminosity at a given temperature than would be expected from extrapolation of the cluster $L : T$ relation (Ponman et al. 1996; Helsdon & Ponman 2000a) and flatter X-ray surface brightness profiles than clusters (Ponman et al. 1999). It has proved instructive to consider these observations in terms of the *entropy* of the gas (Bower 1997; Ponman et al. 1999), which is found to be higher in low mass systems than would be expected from a self-similar scaling of clusters, although the idea of a simple universal “entropy floor” (Ponman et al. 1999) now looks to have been over-simplistic (Pratt & Arnaud 2003; Ponman et al. 2003; Sun et al. 2003; Mushotzky et al. 2003; Voit & Ponman 2003).

A number of mechanisms have been suggested which might account for this behavior of the entropy, by heating of the gas, or removing low entropy gas through cooling, or some combination of the two – a review of these models can be found in Ponman et al. (2003). Irrespective of the means by which the entropy is raised in lower mass systems, the main effect is to reduce the density of the IGM, though its temperature may also be somewhat increased (e.g. Voit et al. 2002). Hence, if this picture for the similarity breaking is basically correct, one would also expect the $L_X : \sigma$ relation (between X-ray luminosity and velocity dispersion) to steepen in galaxy groups, since the reduction in gas density lowers L_X but not σ . However, a variety of studies (e.g. Mulchaey & Zabludoff 1998; Helsdon & Ponman 2000b; Mahdavi et al. 2000) have shown that this is not the case, although more recently Mahdavi & Geller (2001) has argued that there is a continuous, and gradually steepening $L_X : \sigma$ relation from clusters to individual galaxies. Helsdon & Ponman (2000b) assembled a sample of 42 galaxy groups, and derived a slope for the $L_X : \sigma$ relation of between 2.4 ± 0.4

and 4.7 ± 0.9 (depending on how the data were fit). This group slope is flatter (or at least not steeper) than the cluster relation, which has been variously derived as 6.38 ± 0.46 (White et al. 1997), 5.24 ± 0.29 (Wu et al. 1999) and $4.4_{-0.3}^{+0.7}$ (Mahdavi & Geller 2001) – all these results being obtained using orthogonal regression techniques.

A flat $L:\sigma$ relation in groups is also indicated by the independent studies of Mulchaey & Zabludoff (1998) and Mahdavi et al. (2000). The former authors had only a small sample of groups, but derived reliable dispersions for these by enlarging their group membership to $\gtrsim 20$ galaxies via multi-fiber spectroscopy. Mahdavi et al. used ROSAT All Sky Survey data, allowing the study of a large sample of groups, but providing poor quality data (a few hundred seconds exposure) for each one. Hence they were unable to remove X-ray emission arising from individual galaxies within the systems they studied. They derived an $L:\sigma$ relation which flattens drastically to $L_X \propto \sigma^{0.37}$ in the group regime. Unfortunately, it is unclear to what extent this results from contamination of their diffuse emission with flux from individual group galaxies.

Thus, these group studies suggest that the $L_X : \sigma$ relation in groups is actually *flatter* than an extrapolation of the relation for clusters. This surprising result could indicate a possible fundamental flaw in the whole picture whereby the X-ray luminosity in poor systems is suppressed by excess entropy. Alternatively, it might result from the existence of unexpected new sources of X-ray emission in some low velocity dispersion groups. Looking at the group $L_X : \sigma$ relation (e.g. Figure 4 in Helsdon & Ponman 2000b) it is clear that the flat $L_X : \sigma$ relation is driven by the properties of a set of groups with $\sigma \lesssim 110 \text{ km s}^{-1}$ which have diffuse luminosities much greater than the values which would be expected on the basis of the cluster $L:\sigma$ relation ($L_X \ll 10^{41} \text{ erg s}^{-1}$).

In order to better understand the properties of these low velocity dispersion groups we have obtained Chandra data for two of these systems. In section 2 we describe the spatial and spectral analysis, and present some basic properties of these systems. In section 3 we compare the Chandra and ROSAT observations of these systems, and finally we discuss the results in section 4. Throughout this paper we use $H_0 = 75 \text{ km s}^{-1} \text{ Mpc}^{-1}$.

2. Data Reduction and Analysis

We obtained observations of two low velocity dispersion groups, a ~ 20 ksec observation of NGC 1587 on October 3rd 2000, and a ~ 20 ksec observation of NGC 3665 on 3rd November 2001. One point of concern with these two systems is the fact that their velocity dispersions are so low (106 km s^{-1} for NGC 1587 and 29 km s^{-1} for NGC 3665). In their original group

catalogues these systems have had their velocity dispersions estimated from a small number of galaxies. A natural concern is therefore that the anomalous positions of these systems in the $L_X : \sigma$ plot might arise from seriously inaccurate values of σ . However, searching the NED database for additional galaxies lying within 1 Mpc in projection, and 400 km s^{-1} in velocity from the catalogued group centroid, brings the membership to 8 for NGC 1587 and 10 for NGC 3665. While these extra members do tend to increase the calculated dispersions of the groups a little, both these systems still have low velocity dispersions – 108 km s^{-1} for NGC 1587 and 65 km s^{-1} for NGC 3665.

The basic X-ray data reduction was based on the “CIAO science threads” given on the Chandra X-ray Center (CXC) web pages, and is briefly summarised below. All analysis was carried out using CIAO version 2.3, and CALDB version 2.21.

2.1. Initial Reduction

Initially the data were reprocessed to ensure the latest calibration files were used (e.g. gain), and the CTI correction applied. In addition, the ~ 1.5 arc second aspect offset present in some Chandra observation files was corrected. The observation of NGC 3665 was taken in VFAINT mode (NGC 1587 was in FAINT mode), and as a result the VF option was selected for the reprocessing of this dataset as this can significantly reduce the background at low and high energies in VFAINT observations. Following this, the wavdetect tool was used to source search a coarsely binned image and identify obvious sources. These sources were removed from the data and a light-curve was generated from the remaining data. This light-curve was then used to identify and remove periods of high background from the data.

The method used to identify periods of high background depends partly on how subsequent reduction/analysis is to be carried out. In this case, we make extensive use of the blank sky datasets available in the CALDB, and so must clean the data in a manner comparable with the method used for the blank sky files. In this case we actually generate light-curves in two different energy bands — for the FI chips we use a energy band of 0.3-12 keV and for the BI chips we use a band of 2.5-7 keV. These energy bands were selected as these are the bands which best show flares on the two types of chips (see discussion of the ACIS background on the CXC web pages). Light-curve bin lengths of 259.28 seconds were used and a 2.5 sigma clip was applied to remove bad regions of the observation. Note that this is different to the fixed factor of 1.2 used in the analysis thread. The 2.5 sigma clip was used as the expected quiescent scatter of the 2.5-7 keV band for the whole S3 chip is greater than a factor of 1.2. Furthermore, if large regions of the FI chips are excluded (due to sources for example) then the expected scatter from the FI chips can also exceed the factor of 1.2. In cases like this the

blank sky “cookbook” recommends extending the bin length so that the expected scatter is less than a factor of 1.2. Instead we have used a cut based on the observed scatter which should have a similar effect.

After identifying times of bad data, the data were filtered on both the good time intervals inferred from the BI and FI chips. This was done so as to be as careful as possible to exclude possible flares from the data. For NGC 1587 the final exposure time was \sim 19 ksec and for NGC 3665 \sim 17 ksec. Finally, the appropriate blank sky files for the observations were identified. It was checked that the same calibration files (e.g. gain) were used for the background files as for the data, and the background datasets were then reprojected to have the same pointing as the groups observations.

In Figure 1 adaptively smoothed X-ray contours (in the 0.7 - 1.5 keV band) are overlaid onto a digital sky survey image for both of the systems. The smoothing was carried out with a gaussian filter whose sigma was adjusted to be 2/3 the radius needed to include a minimum of 25 counts in a circle around each pixel. After examining these images and also 1D profiles of the ratio of data to background, circular regions were selected in which to carry out further data analysis (e.g. spectral and spatial analysis). These regions are also marked in Figure 1. For NGC 1587 the region of interest is a circle of radius 4.5 arcmin and for NGC 3665, a circle of radius 5.8 arcmin.

The blank sky datasets were also checked to see if they were a good representation of the real background in the target observations. The X-ray contour maps were used to identify several regions where there were apparently no sources. In each of these regions the observed counts in several different energy bands were compared with the predicted counts from the blank sky datasets in the same region. These checks showed that the predicted background was indeed consistent with that observed.

2.2. Spectral Analysis

As we are primarily interested in the diffuse emission from these targets it is important to remove any contaminating sources. The wavdetect tool in CIAO was used to source search a full resolution image. The identified sources were examined in ds9 to ensure all obvious contaminating sources were identified and that a significant fraction of the diffuse emission was not removed (e.g. check that a large part of the group central region was not removed as a “contaminating source”). All events associated with these sources were then removed from the data along with all data outside the region of interest (described in the previous section).

Weighted spectral responses for the data were then generated. The 0.5-2keV band was selected for the weight map as this produces a map that should more closely follow the distribution of source counts (most source counts fall in this band and a harder map would tend towards an area weighting). Unfortunately, it turns out that in the detection radius for these two groups, the background still dominates over the source counts. It is not possible to do a simple background subtraction to recover the source counts distribution, as the average background counts per pixel is low (~ 0.03 counts per pixel in the blank sky files), and subtracting this number from the detected source counts (which have a minimum value of 1) will not have much effect on the distribution (given that negative weights are correctly ignored).

In order to recover the approximate background subtracted spatial source distribution, an image of the data and background (normalized to the same exposure time as the data) are adaptively smoothed with a top hat filter, which varies in size to include 10 counts in total. This smooth also records for each pixel the area needed to include these 10 counts. For each pixel, by comparing the area needed in the background image with the area needed in the source image, it is possible to obtain an estimate of the ratio of source flux to background flux. Given this ratio, and an estimate of the background, it is possible to recover an estimate of the source distribution. This estimate of the source distribution was then used to generate the weighted responses. The resultant effective area file was also corrected for the time dependent reduction in the ACIS low energy quantum efficiency using the tool, `corrarf`, available on the CXC web pages.

Source and blank sky spectra were extracted in the region of interest. The source spectra were grouped to give a minimum of 20 counts in each bin (to allow χ^2 fitting later). The background subtracted data were then fit to a MEKAL plasma model in `sherpa` (Freeman et al. 2001). The fit was restricted to the range 0.5-2.5keV, as there may be calibration problems below 0.5 keV and the source counts had dropped to essentially zero by 2.5 keV in these systems. The Hydrogen column density in these fits was fixed at a value determined from radio surveys (Dickey & Lockman 1990). An example spectrum and fit, is shown in Figure 2. Overall, there were approximately 750 net source counts for NGC 1587 and approximately 650 for NGC 3665.

After fitting the data, the best fit model was used to generate a spectral weights file, which contains the fraction of the incident flux falling in a series of energy bands. This can then be used to refine the spectral fit — the weighted spectral responses generated initially are based on using the detected counts to weight the responses, whereas, in reality, the incident flux should be used. A spectral weights file can be used to correct the detected counts to give the incident flux, which can then be used to generate the weighted responses

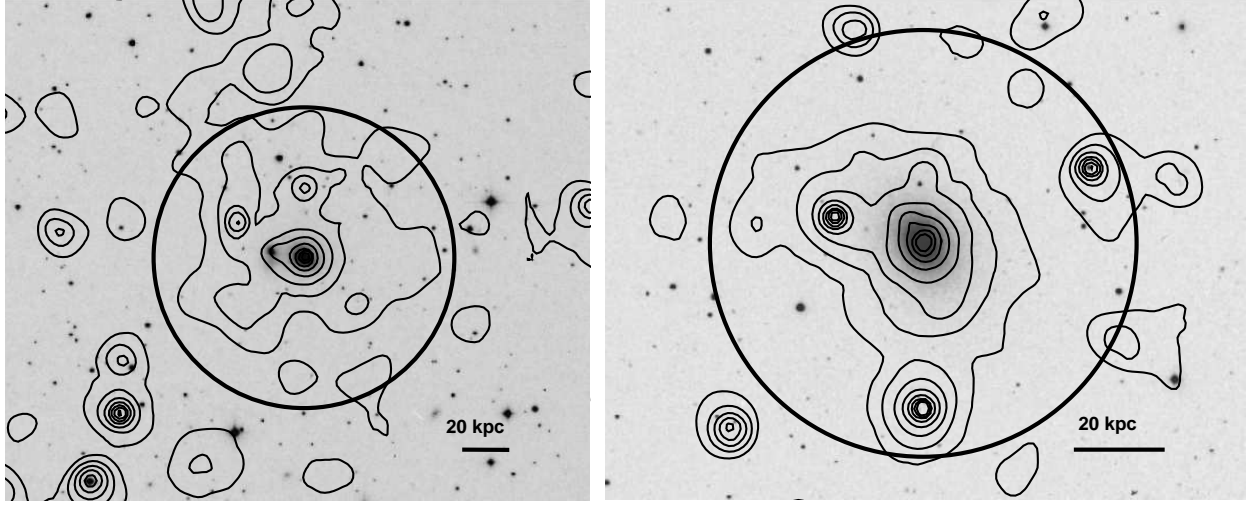


Fig. 1.— Adaptively smoothed X-ray contours in the 0.7 - 1.5 keV band overlaid onto DSS images, for NGC 1587 (left) and NGC 3665 (right). The lowest contour is 5 sigma above the background and the remaining contours are logarithmically spaced beginning with 10 sigma, 20 sigma, 40 sigma, etc. The circles show the radii used for analysis of the systems.

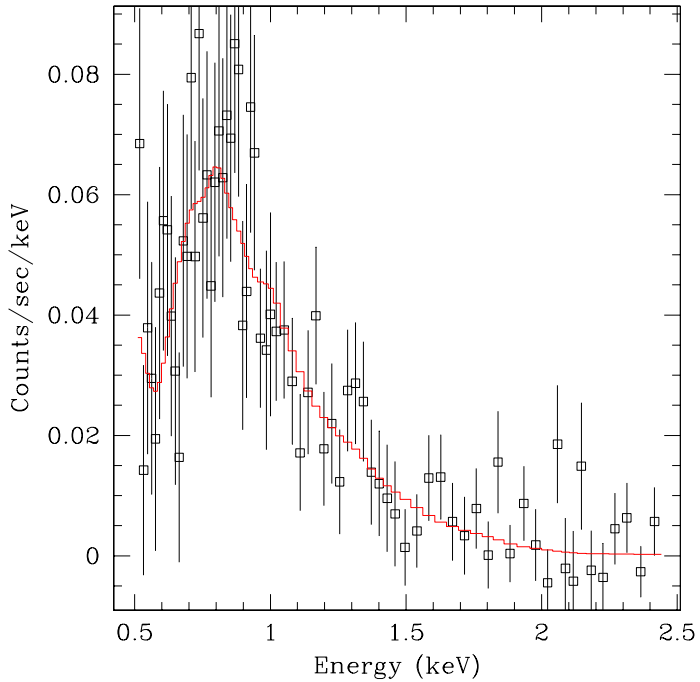


Fig. 2.— Example spectral fit for NGC1587 with the Abundance free.

(Note that this is discussed in the CXC analysis thread on weighting ARFs and RMFs). Updated spectral response files were then generated and the spectral data were refit. This iterative process was then repeated until the best fit spectral model stabilized (less than a 1% change in best fit temperature and also the lower bound temperature error was the stable criteria). For both the groups in this work a stable solution was reached after just two iterations. The best fitting models for the two groups are given in Table 1 along with the inferred luminosities. The luminosities quoted are to the radius of data extraction and include a small (<2%) correction for diffuse flux which was removed when excluding other sources. This correction was calculated by comparing spatial models (described below) with and without sources removed. Errors on the luminosities are derived using a Monte Carlo method. A series of spectral models was generated, with a range of temperatures and abundances, extracted at random from a gaussian distribution centered on the best fit value, and with standard deviation corresponding to the 1σ errors. Each model was then refit to determine the normalisation and a corresponding flux. The standard deviation of the fluxes was then used to infer the error on the luminosity.

We were also interested in looking for potential radial temperature and/or metallicity variations in these systems. As a result, spectra were extracted in a series of annuli, ~ 1 arcmin in width, for each system. We then used the procedure described above for the total group emission to fit the spectral data in each annular bin. The only difference from the earlier process was to use the spectral weights file from the integrated group fit for each of the annular bins, rather than running the full iterative process on each annular bin. A test case was run on one of the annuli which confirmed that this did not significantly alter the results. The projected 2D temperature profiles are shown in Figure 3. The abundance profiles are not shown, as outside of the central bin the abundance was poorly constrained. For the remainder of this paper, unless explicitly stated otherwise, we use an abundance fixed at the global value. Fixing the abundance at the global value does not have a significant impact on the derived 2D temperature profiles, as can be seen in Figure 3.

Finally, we also carried out a 3D deprojection of the spectral data in each annulus. In reality the spectral data for each of the 2D annuli has some contribution from gas which lies at a larger 3D radius, but which is projected onto a smaller radius when viewed. We attempt to correct for the effects of this, by deprojecting the data using an “onion skin” method. Starting with the outer shell (which in theory should have no other emission projected onto it), and assuming spherical symmetry, it is possible to calculate what fraction of the volume of the 3D shell is seen, and to calculate what fraction of this outer shell is projected onto all inner annuli. It is then possible to construct a series of spectral models which describe the contribution from this outer 3D shell to each 2D annulus. In each model, all parameters apart from the normalisation are fixed at the same values and the volume factors can be

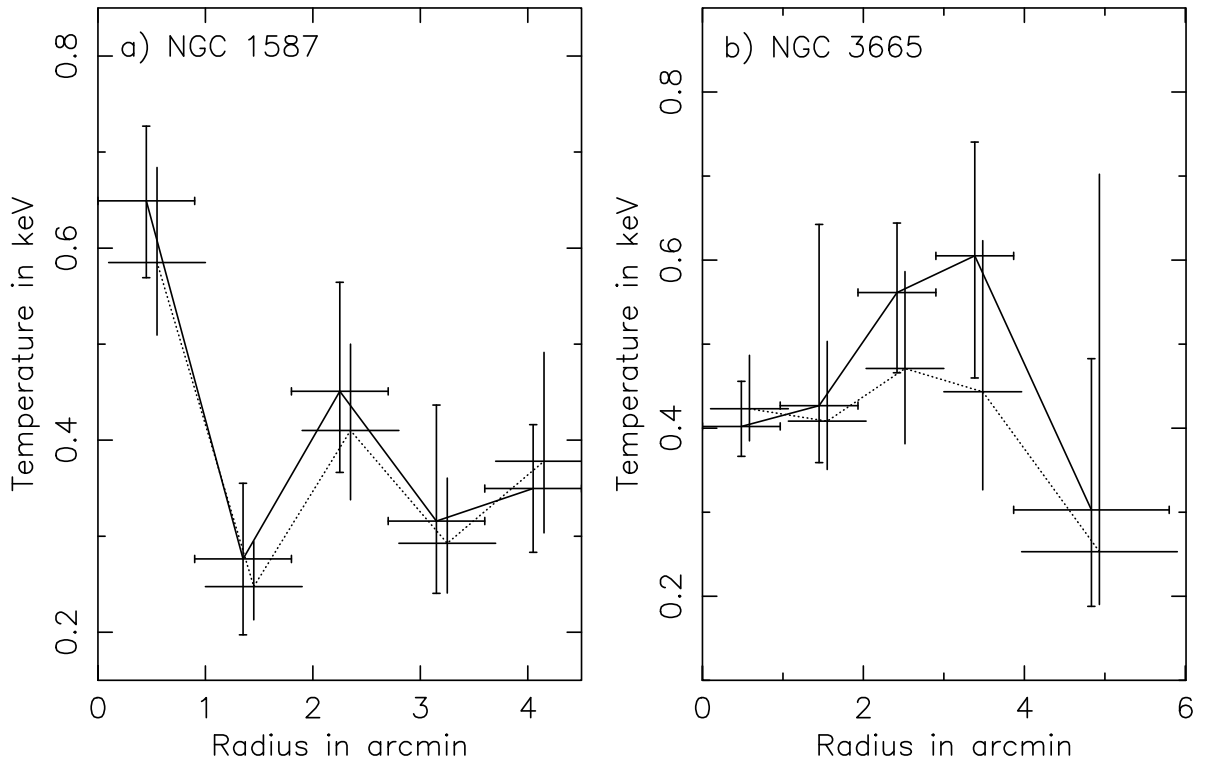


Fig. 3.— 2D temperature profiles for both a) NGC 1587 and b) NGC3665. Barred crosses and solid line represent the profile obtained with the metallicity allowed to vary for each annulus, while the plain crosses and dotted line mark the profiles obtained with the metallicity fixed at the global value. Note that the fixed metallicity points have been offset slightly on the radius axis so as to show the error bars more clearly.

used to fix the relative normalisations of the models. This procedure can then be repeated for all inner annuli. Thus the spectral data for any particular 2D annulus is comprised of contributions from the model describing the 3D shell at this radius, plus contributions from all overlying shells.

All spectra (and appropriate responses) for each annulus were then simultaneously fit to the described set of spectral models. This gave a set of models describing the 3D spectral properties of the gas. As well as allowing the temperature and metallicity to vary separately in each shell, models were fit which constrained both the temperature and metallicity to a simple linear profile with radius. The advantage of using linear models for the temperature and abundance is that it enables a better impression of rough radial trends in low count data. This is because only 2 parameters are fitted (central value and gradient) rather than N parameters, where N is the number of radial annuli. The deprojected temperature profiles are shown in Figure 4 and the parameters for the linear temperature and abundance fits are given in Table 2. Note that these radial profiles only cover the inner regions of these groups, and that it is not sensible to extrapolate them substantially (for example, to the Virial radius), as the extrapolated profiles may become unphysical (e.g. negative temperature). It is also worth noting that by looking at Figure 4 one can see that neither group is significantly non-isothermal apart from the central point in NGC 1587.

2.3. Spatial Analysis

As for the spectral analysis, we are interested in the properties of the diffuse gas, so all other contaminating sources were removed, along with all data outside our main region of interest. An image was then generated in the 0.7-1.5keV band. This particular band was chosen to help maximise the signal to noise ratio of the data. As well as this image, two other important sets of information are needed: an exposure map and a background model. The exposure map takes into account potential exposure variations across the region of interest. As a result an exposure map was generated, using the standard CIAO tools and the spectral weights file derived from the best fitting integrated group spectral model. We also removed (set to zero) regions of the exposure map where sources had been removed in the group image.

Ideally, if the sky background is flat, the detector background should have the same shape as the exposure map. However comparison of the blank sky datasets in the 0.7-1.5 keV band with the exposure maps, shows that there are gradients in the background level across a chip, which are greater than would be expected from the exposure map alone (by a factor of ~ 5 in the worst case). These variations are most likely due to variations in the

Table 1. Results of Spectral fitting to group emission.

Group	N_H 10^{22} cm^{-2}	Temperature (keV)	Abundance (Solar)	χ^2/dof	Distance (Mpc)	$\log L_X$ (erg s^{-1})
NGC 1587	0.0685	$0.37^{+0.04}_{-0.04}$	$0.012^{+0.012}_{-0.009}$	49.76/69	48.8	$41.22^{+0.05}_{-0.04}$
NGC 1587	0.0685	$0.53^{+0.07}_{-0.04}$	(0.3)	72.76/70	48.8	$40.88^{+0.01}_{-0.01}$
NGC 3665	0.0206	$0.45^{+0.07}_{-0.04}$	$0.04^{+0.02}_{-0.01}$	92.84/71	27.8	$40.58^{+0.05}_{-0.04}$
NGC 3665	0.0206	$0.52^{+0.06}_{-0.04}$	(0.3)	106.18/72	27.8	$40.37^{+0.01}_{-0.01}$

Note. — All errors are 1σ . Luminosities are absorption corrected, bolometric and assume $H_0 = 75 \text{ km s}^{-1}$.

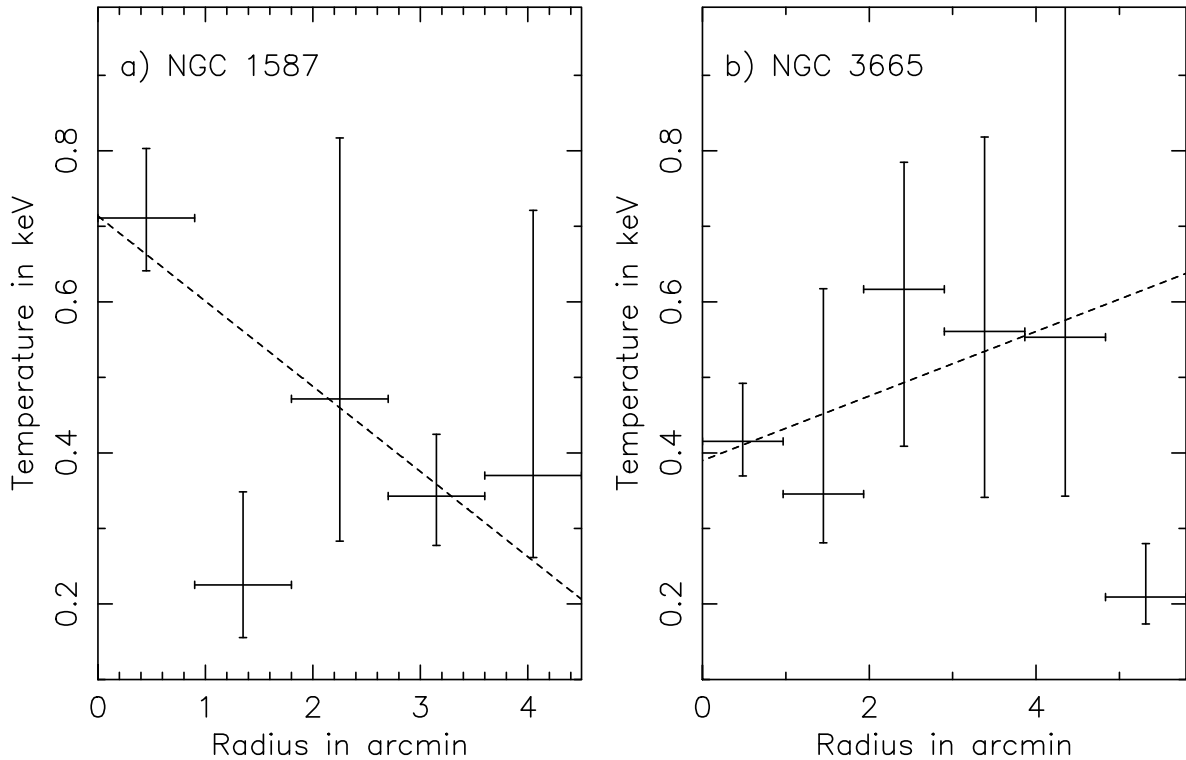


Fig. 4.— Deprojected 3D temperature profiles for both a) NGC 1587 and b) NGC 3665. The dashed line represents the profile obtained if the temperature is constrained to be a linear function with radius during fitting.

cosmic ray component of the background (e.g. see the discussion of the ACIS background on the CXC web pages). It is important to allow for these variations, as the diffuse group emission may be at a level close to that of the background. To do this, a carefully smoothed version of the blank sky image was used to correct an exposure map image for the effects of this gradient. The reason a corrected exposure map was used as the basis of the background, rather than just the smoothed blank sky images, relates to the procedure used to infer the shape of the background. To produce a smoothly varying background from the blank sky files, they first had to be binned up to a much coarser resolution, after which two different smoothing algorithms were used to infer the structure of the background over a chip. This smoothing has the side-effect of effectively adding in extra counts outside the boundaries of the chips, which are not wanted. Using this smoothed image to correct an exposure map automatically removes these extra counts (because the exposure map is zero at those points).

This gave a reasonably smooth background image, with an overall shape the same as that observed in the blank sky dataset. The real blank sky dataset was then used to predict the overall background for the group observation, and the background model was renormalised to match this prediction. This gave a background image with the correct shape and normalisation for the observation. Finally, this background image was divided by the exposure map to produce an exposure corrected background model, which would be used as a model component in Sherpa.

When modelling the diffuse emission, all fits are done with 2D data. Although 1D profile fits would be simpler to derive, they suffer from potentially serious biases relating to where the profile is centered, and the effects of possible ellipticity of the emission (Helsdon & Ponman 2000a). To speed up the 2D fitting process, images, exposure maps and background models were actually generated for three different bin sizes covering different regions - for data within 1 arcmin of the center a bin size of ~ 2 arcsec was used, for data between the

Table 2. Results of the deprojection analysis, with both the Temperature (T) and abundance (Z) profiles constrained to be simple linear models.

Group	T_0 (keV)	dT/dr (keV/arcmin)	Z_0 (Solar units)	dZ/dr (Solar units/arcmin)
NGC 1587	$0.712^{+0.073}_{-0.086}$	$-0.112^{+0.035}_{-0.023}$	$0.118^{+0.072}_{-0.049}$	$-0.031^{+0.018}_{-0.018}$
NGC 3665	$0.390^{+0.071}_{-0.052}$	$0.043^{+0.030}_{-0.031}$	$0.000^{+0.019}_{-0.059}$	$0.042^{+0.023}_{-0.017}$

Note. — Negative values for the gradients indicate a profile dropping with increasing radius.

radii of 1 and 3 arcmin a bin size of ~ 10 arcsec was used, and for radii beyond 3 arcmin a bin size of ~ 30 arcsec was used. Thus at larger radii (and lower counts) a larger bin size was used. This prevented the fitting process from being too slow, whilst still allowing good resolution in the central regions, which was important for getting good constraints on the fitted models. The data were then input to Sherpa and fit in 2D with β models of the form:

$$\Sigma(r) = \Sigma_0(1 + (r/r_{core})^2)^{-3\beta_{fit}+0.5} + B \quad (1)$$

where the free parameters were the central surface brightness Σ_0 , the core radius r_{core} , the index β_{fit} and the x and y position of the center of the emission. Note that models for the different resolutions were linked together as appropriate. Both spherical and elliptical fits were carried out on the data, with the ellipticity and the position angle being extra free parameters in the elliptical fits. The background component, B was also present in all fits, and it was defined by a gridmodel component derived from the exposure corrected background model image generated earlier. Note that this background component was not free to vary. Given that the cosmic ray background can vary from one observation to another, test fits in which the background amplitude was allowed to vary, showed that while both the core radius and beta increase (by about 10% for beta), the new values and associated errors were consistent, at approximately the one sigma level, with the original values in which the background was frozen.

Many groups are observed to have 2 components present in their X-ray emission (e.g. Mulchaey & Zabludoff 1998; Helsdon & Ponman 2000a), and we attempted to fit both one and two component β models to the data. Unfortunately, the data for these two systems were not sufficient to provide robust constraints on any reasonable two component fits, so it was only possible to derive reliable one component fits. The results of the 2D fitting are shown in Table 3. These results are for spherical β models. Elliptical β models were also fit to the data, but in both cases it was found that the fit statistic did not improve significantly for the extra parameters.

The Cash statistic (Cash 1979) was used when minimising the 2D fits. On its own this statistic does not give any indication of the quality of fit, and it was originally intended to determine the quality of fit using a Monte Carlo procedure similar to that used in Helsdon & Ponman (2000a). Using this method, estimates of the quality of the fit were obtained by using the best fit model to generate 1000 model datasets with added poisson noise. The Cash statistic of each of these noisy datasets when compared with the best fit model was then calculated, giving the expected distribution of the Cash statistic for the best fit model. The real Cash statistic for the data was then compared with this distribution, by for example, calculating the number of standard deviations the real Cash value lay from the mean of the 1000 noisy models distribution. Unfortunately, it has now become apparent that this

procedure suffers from some serious flaws. Most notably, the quality of fit obtained depends significantly on the binning of the data.

2.3.1. Problems with testing fit quality

To illustrate the problem with this method, consider the simple toy problem of a 256x256 image, with 20 counts in each pixel, apart from a 50 pixel wide bar running up the image with 20.8 counts per pixel. This represents the correct model of the data, from which can be generated 'observed' datasets by adding in poisson noise. Given some 'observed' data, is it then possible to distinguish between the datasets and a flat model with a value of ~ 20.16 counts per pixel (this level is equal to the average number of counts per pixel in the original model)? The Monte Carlo method described above was used on the 256x256 image and also repeated with the data re-binned by a factor of 2, 4 and 8 (i.e. 128x128, 64x64, 32x32, with the overall counts in the image the same in each case). For the 256x256 case the Monte Carlo method suggests that the flat model is a perfectly reasonable fit to the data generated with the bar model (the 'observed' Cash value lies 0.86σ from the distribution mean). For the 128x128 case, the flat model is found to be a borderline acceptable fit (1.83σ), for 64x64 the flat model is ruled out (3.43σ), and for the 32x32 case it is strongly ruled out (6.65 sigma offset). It should also be pointed out that this effect is not limited to the Cash statistic alone, as nearly identical results are obtained using χ^2 statistics.

This shows that in the above case, the higher resolution data is more likely to be considered an acceptable fit. The main reason for this is that the width of the statistic distribution generated from the 1000 random realizations increases roughly as the square root of the number of pixels, while the size of the mismatch between the 'real' statistic value and the distribution mean is approximately constant. This dependence on resolution is clearly an undesirable property when trying to construct a reliable estimate of the quality of fit.

The origin of this effect can be quite easily understood. When using either the Cash statistic or the χ^2 statistic, the value of the statistic is derived from the addition of scaled residuals, without any account of the *spatial structure* of these deviations. For example, consider the implications of structure in these deviations in the case of the χ^2 statistic, where the maths is simpler. For a good model, data residuals (data, d_i , minus model, m_i) are uncorrelated from one point to the next. This is clearly not the case in the above toy problem, as there is a systematic offset across the image. Systematic offsets could also arise very easily in surface brightness profile analyses. To see the effect of systematic offsets on the χ^2 statistic consider the following:

$$\chi^2 = \sum_i \frac{r_i^2}{d_i}, \quad (2)$$

where $r_i = d_i - m_i$. Now r_i can be decomposed into a statistical contribution e_i , with an expectation value of zero, but with $\langle e_i^2 \rangle = m_i$, and a systematic misfit contribution s_i , which is due to real discrepancies between the data and the model.

$$\chi^2 = \sum \frac{e_i^2 + s_i^2 + 2e_i s_i}{d_i} \quad (3)$$

Now suppose that the number of bins is increased by a factor f , without changing the total number of counts. Then the values of d_i and m_i drop by the factor f . Taking expectation values throughout the above expression for χ^2 , the sum runs over fN values, $\langle e_i^2 \rangle$ and d_i both scale as $1/f$, s_i^2 scales as $1/f^2$, and $\langle e_i s_i \rangle$ vanishes. This shows that the contribution to χ^2 coming from the model misfit stays constant, whilst the contribution to χ^2 from statistical variations, and the number of degrees of freedom, scale up as f . Since the width of the χ^2 distribution scales as approximately the square root of the number of degrees of freedom, this means that the significance of the misfit will drop for the higher resolution data (or conversely, binning up the data is more likely to show a misfit), just as seen in the above example. The same effect also exists for the Cash statistic. It is also worth emphasising that this resolution dependence only occurs if there is systematic structure in the residuals. If the residuals do not show any systematic structure the s_i^2 term will scale as $1/f$ and the resolution dependence will disappear. e.g. if in our simple toy model above we had distributed the pixels with 20.8 counts randomly about the image, rather than grouped together in a bar, we would not expect to see the fit quality get worse as the data are binned up (as is the case when they are in a bar). Running the same test as was applied to the image with a bar confirms this prediction – in this case the fit is acceptable at all resolutions (always $< 1\sigma$ from the distribution mean).

The resolution dependence of the fit statistic above is a demonstration that simple misfit tests based on the value of the Cash or χ^2 statistics do not take into account the effects of spatial correlations between residuals. In particular, this means that in the limit of very fine binning, the misfit test is a very weak measure of goodness of fit. As larger bins are used, spatially correlated residuals combine to become more significant, but ultimately all structure will be lost in the limit of very coarse binning – in the limit of a single bin, if the model and data have the same overall normalization, a perfect fit will always be obtained, regardless of the smaller scale structure of the model and data. Given this, a reasonable compromise approach is to bin on progressively larger scales, and to take the case where the fit is poorest as an indication of the true quality of fit of the model. However, this is still

not ideal, since the scale of the systematic misfits could vary around the image, so that no single binning scale is entirely satisfactory. It should also be noted that these results are quite general, and apply, for example, to the use of χ^2 to evaluate the adequacy of *spectral* fits.

The problems described above make it difficult to reliably estimate the quality of our spatial fits. Running the 2D data for the two groups through the flawed test described above suggests that the circular beta models are acceptable fits. Running the quality of fit test at a variety of resolutions (binning the data by factors of 1, 2, 4, 8 and 16) suggests that there is systematic structure in the data minus model residuals of both groups (i.e. the quality of fit gets worse as the data are binned up). At the worse fit quality both groups are still acceptable fits although only marginally so for NGC 1587 with a worse case offset of 1.99σ , while NGC 3665 has a worse case offset of 0.5σ . However this result should be treated with some care given the limits and reliability of the quality of fit test. It is however, reassuring to note that the 1D profiles (projected from 2D) shown in Figure 5 suggest that the models do appear to provide a reasonable match to the data.

3. Comparison with previous ROSAT observations

The spectral parameters as derived for these groups are compared with previous ROSAT determinations in Table 4. The Chandra derived parameters have a number of differences from the ROSAT values: The temperature for NGC 1587 is much lower than the ROSAT data had suggested, while the derived bolometric luminosity is consistent with previous estimates (although both are dependent on the abundance). In contrast the X-ray temperature of NGC 3665 is comparable to previous estimates and the Chandra derived X-ray luminosity is a little lower. The ROSAT observations were generally unable to put any strong constraints on the abundances, so no meaningful comparison of the abundances is possible.

Given that there are clearly differences seen, it is important to try to understand their origin. A likely reason is that the ROSAT data have been contaminated by unresolved

Table 3. Results of fitting a single beta model to the spatial emission.

Group	β_{fit}	Core radius (arcsec)	Core radius (kpc)
NGC 1587	$0.36^{+0.01}_{-0.01}$	<1	<0.24
NGC 3665	$0.46^{+0.02}_{-0.02}$	$6.1^{+1.7}_{-1.6}$	$0.83^{+0.23}_{-0.22}$

Table 4. Comparison of the X-ray spectral parameters derived in this *Chandra* study with those from previous *ROSAT* studies.

Instrument	Temperature (keV)	Abundance (Solar)	$\log L_X$ (erg s $^{-1}$)	Reference
NGC 1587				
<i>Chandra</i>	$0.37^{+0.04}_{-0.04}$	$0.012^{+0.012}_{-0.009}$	$41.22^{+0.05}_{-0.04}$	1
<i>Chandra</i>	$0.53^{+0.07}_{-0.04}$	0.3 (fixed)	$40.88^{+0.01}_{-0.01}$	1
<i>ROSAT</i>	0.92 ± 0.15	0.3 (fixed)	41.10 ± 0.18	2
<i>ROSAT</i>	$0.90^{+0.81*}_{-0.46}$	0.3 (fixed)	$41.18^{+0.13*}_{-0.41}$	3
NGC 3665				
<i>Chandra</i>	$0.45^{+0.07}_{-0.04}$	$0.04^{+0.02}_{-0.01}$	$40.58^{+0.05}_{-0.04}$	1
<i>Chandra</i>	$0.52^{+0.06}_{-0.04}$	0.3 (fixed)	$40.37^{+0.01}_{-0.01}$	1
<i>ROSAT</i>	0.45 ± 0.11	0.17 ± 0.14	40.81 ± 0.1	2
<i>ROSAT</i>	$0.33^{+0.14*}_{-0.07}$	0.3 (fixed)	$40.77^{+0.37*}_{-0.47}$	3

Note. — *ROSAT* Luminosities have been corrected to the exactly the same distances used in this work. Errors are 1 sigma unless marked with a * in which case they represent 90% confidence limits.

References. — (1) This Work, (2) Helsdon & Ponman (2000a), (3) Mulchaey et al. (2003)

point sources which have been identified and removed in the Chandra data. To check for this we first calculated the total background subtracted counts in the Chandra data after removing all identified contaminating sources. These counts were calculated in the ROSAT bandpass (0.3–2.3 keV) and over the same area that the ROSAT data were derived (a 6 arcminute radius circle in both cases, with an additional region excluded in NGC1587 where the ROSAT PSPC support ring fell in the area). The contaminating source list from Chandra was then compared with the equivalent list for the ROSAT data (from the analysis of Helsdon & Ponman 2000a), and the Chandra sources corresponding to sources found in the ROSAT data were identified. The background subtracted counts in the Chandra data were then re-calculated but this time, only the ROSAT identified sources were removed. The results of these calculations for the two groups are shown in Table 5.

Table 5 shows that for both groups there is clearly substantial contamination of the ROSAT data due to unresolved point sources. For these groups unresolved point sources have increased the real (Chandra measured) flux by 30–40% in the ROSAT data. Taking into account these unresolved point sources moves the ROSAT derived luminosities for NGC 3665 into better agreement with the Chandra data, whilst for NGC 1587 the ROSAT luminosities drop relative to the Chandra luminosity. However the luminosities can also be significantly altered due to differences in the spectral properties (in particular the temperature). These luminosities are based on unabsorbed fluxes, and the correction from an absorbed flux to unabsorbed flux tends to be larger for cooler systems. For NGC1587 this effect increases the luminosity by a factor of ~ 1.4 (for a spectral model with $T = 0.9$ keV changing to a model with $T = 0.37$ keV), which almost exactly cancels out the effect of the unresolved point sources, resulting in a similar final luminosity to that derived in the ROSAT data. Note that the hotter temperature obtained when fixing the abundance at 0.3 results in a luminosity lower than that obtained with the ROSAT data.

For NGC 3665 the luminosity change due to the spectral model differences is a factor of ~ 1.2 which again acts to reduce the difference between the ROSAT and Chandra data, with the end result that after allowing for both this correction and the correction for unresolved point sources, that the Chandra derived luminosity is a little below the ROSAT luminosity, but probably just consistent within the errors. The difference in luminosity between the Chandra data with free and fixed abundances, is again due to the differences in the spectral models.

One final check that can be carried out on the spectral data is to examine whether the unresolved point sources in the ROSAT data can explain the spectral differences seen in the different instruments. To check this, the integrated group spectra for each group were refit, but this time only removing those Chandra sources also identified in the ROSAT data. For

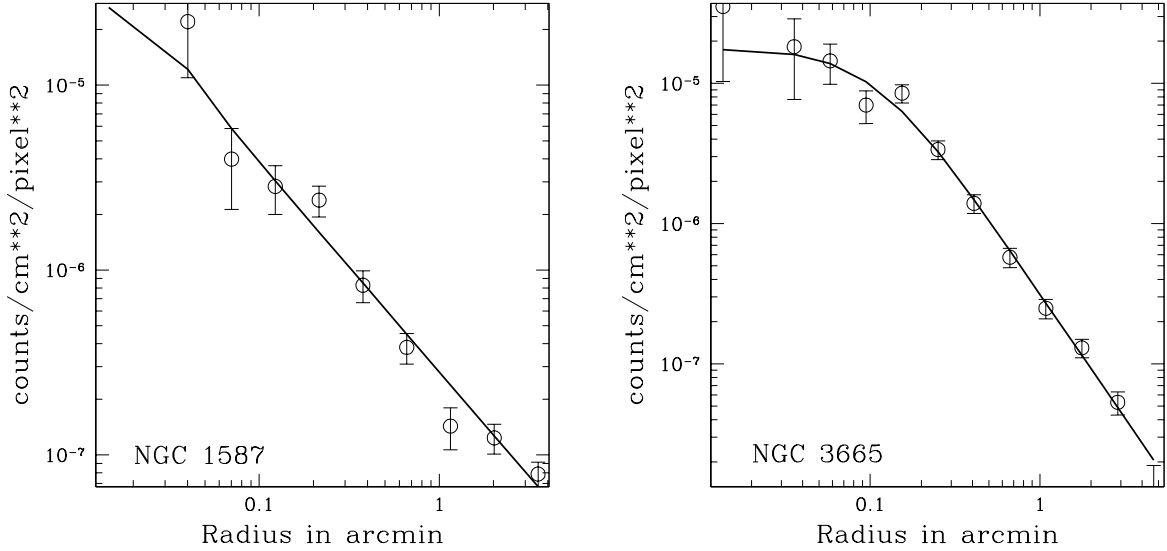


Fig. 5.— 1D background subtracted surface brightness profiles (projected from 2D) of NGC 1587 (left) and NGC 3665 (right).

Table 5. Net *Chandra* counts in the 0.3-2.3 keV band, over approximately the same region the *ROSAT* data were extracted. The columns show firstly the net counts after removing all contaminating sources as identified by the *Chandra* data, then the net counts obtained if only sources also identified in the *ROSAT* data are excluded. The final column shows the ratio between these two numbers, and gives an indication of the fraction of the original *ROSAT* flux due to unresolved contaminating point sources.

Group	Chandra identified sources removed	ROSAT identified sources removed	Factor difference
NGC 1587	616 ± 67	802 ± 68	1.30
NGC 3665	666 ± 62	936 ± 64	1.41

both groups the effect of this was to raise the fitted temperature a little, to $T = 0.46^{+0.06}_{-0.09}$ for NGC 1587 and $T = 0.49^{+0.05}_{-0.04}$ for NGC 3665 (abundance free in both cases). With these sources added back in, the luminosity for NGC 3665 moves into very good agreement with the ROSAT derived values, while the luminosity of NGC 1587 drops a little due to the change in spectral parameters.

In summary, adding back unresolved ROSAT sources into the Chandra data results in good agreement between the temperature and luminosity for NGC 3665. However, for NGC 1587, the temperatures are still lower than the best fit ROSAT temperature, although this difference is reduced if a fixed abundance of 0.3 is used, as with the ROSAT data.

Table 6 compares the spatial parameters derived for the Chandra data with those obtained in previous ROSAT analyses. As can be seen the β_{fit} values are roughly consistent with previous ROSAT values, as are the core radii, although these are constrained much more tightly in the higher resolution Chandra data. For NGC 1587, the core radius is much smaller than that obtained with ROSAT, although the ROSAT values are not particularly well constrained, and the difference is not significant. The slightly lower β_{fit} value for NGC 1587 is most likely related to the smaller core radius as there is a well known correlation between core radius and β_{fit} in these models.

4. Discussion

Our primary result is that the bulk of the “diffuse” emission reported from the ROSAT analyses of these two very low velocity dispersion groups is confirmed by Chandra to be genuine hot plasma emission from a hot IGM. Nonetheless, we find some significant differences between the ROSAT and Chandra results for these two groups. These discrepancies appear to be primarily related to the effects of contaminating point sources which are not resolved in the ROSAT data. For these two groups these unresolved point sources cause the

Table 6. spatial comparisons

NGC 1587	β_{fit}	core radius arcsec	NGC 3665	β_{fit}	core radius arcsec
<i>Chandra</i>	$0.36^{+0.01}_{-0.01}$	<1	<i>Chandra</i>	$0.46^{+0.02}_{-0.02}$	$6.1^{+1.7}_{-1.6}$
<i>ROSAT HP00</i>	0.47 ± 0.06	20.4 ± 16.2	<i>ROSAT HP00</i>	0.49 ± 0.03	7.8 ± 7.2
<i>ROSAT MDMB</i>	0.42 ± 0.02	<6	<i>ROSAT MDMB</i>	0.42 ± 0.03	<6

ROSAT count rates to be overestimated by a factor of 1.3-1.4, and it should be reasonable to expect other low luminosity ($\log L_X \lesssim 41.5$) groups observed by ROSAT to show comparable contamination. The remaining emission from these systems appears to mostly arise from a hot gas component. The expected discrete source contribution from X-ray binaries in the galaxies of these groups, is a factor of 7-10 times fainter than the measured luminosities (assuming a discrete $L_X/L_B = 29.5 \text{ erg s}^{-1} L_\odot^{-1}$ — O’Sullivan et al. 2001), and would in any case be restricted within the optical confines of the galaxies.

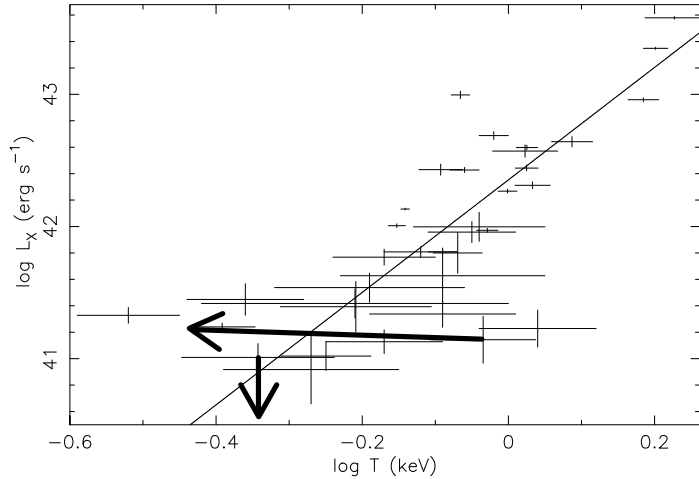


Fig. 6.— The $L_X : T$ relation from Helsdon & Ponman (2000b) with arrows showing how NGC 1587 and NGC 3665 have moved as a result of the analysis in this paper.

For a fixed spectral model, the removal of these point sources in the Chandra data should result in lower group X-ray luminosities. However, significant differences in the fitted spectral models (e.g. a large change in temperature), may act to either increase or reduce the overall effect on the inferred bolometric X-ray luminosity. In general, the properties we derive for these two groups fall within the spread of other groups (e.g. Mulchaey et al. 1996; Helsdon & Ponman 2000a; Mulchaey et al. 2003), although they are amongst the faintest and coolest groups currently known. For example, despite the large change in temperature for NGC 1587, and the drop in luminosity for NGC 3665, the groups still appear to be consistent with previously derived scaling relations such as the $L_X : T$ relation, as shown in Figure 6. This suggests that their dynamical status is not likely to be grossly different from that of other groups.

The low β_{fit} values obtained are consistent with what has been seen in other groups (Helsdon & Ponman 2000a; Mulchaey et al. 2003; Osmond & Ponman 2003), and are broadly consistent with what would be expected, given the possible trends of β_{fit} with temperature

that have been reported (e.g. Helsdon & Ponman 2000a; Sanderson et al. 2003). As for the core radii of these two systems, the Chandra data are able to put much stronger constraints on this parameter than the ROSAT data. One of the problems in previous ROSAT observations of groups (e.g. Helsdon & Ponman 2000a; Mulchaey et al. 2003) is that often the core radii have been unresolved. The Chandra data have enabled us to derive tight constraints on the core radius of NGC 3665, but, remarkably, the core radius for NGC1587 is still unresolved in the Chandra data, implying a power-law like surface brightness profile to within ~ 0.5 kpc of the center of the system.

One might expect these results for beta and core radius ought to be fairly reliable, since the data for these two systems are fit over a region 60 to 130 times larger than the implied core radius. However some caution is needed, as it is possible that there may be a significant bias in these results. In general, groups with good data quality require a 2-component model to adequately describe their surface brightness profiles (Mulchaey & Zabludoff 1998; Helsdon & Ponman 2000a). Unfortunately, the Chandra data for NGC 1587 and NGC 3665 are not of sufficient quality to be able to constrain a 2-component model, or rule out the need for one. Where systems really are described by a 2-component model, the use of a single component model can result in a significant bias in the fitted parameters, in particular β_{fit} may be either under- or over-estimated (Helsdon & Ponman 2000a).

A second potential problem with the issue of fitted surface brightness profiles is the effect of aperture. Simulations of clusters generally produce convex gas density profiles, and as a result the β_{fit} value derived for a surface brightness profile may depend strongly on the range of radii used in the fit (Navarro et al. 1995; Bartelmann & Steinmetz 1996; Voit et al. 2002). In particular, β_{fit} values derived on scales much less than the virial radius tend to be systematically low. This could be a significant problem for both our groups, as they are both detected to only ~ 0.1 -0.2 of their virial radius (R_{200}). However, such simulations are by no means guaranteed to include the correct gas physics, so one would like to appeal directly to observations on the question of whether gas density profiles follow a power law at large radii. Recent XMM observations of two richer galaxy groups (Rasmussen & Ponman 2003), in which X-ray emission is traced to $\sim 0.65R_{200}$, are encouraging, in that a beta model is found to provide a good representation of the profiles to the edge of the data, with no significant convexity in the measured profiles.

Assuming that our surface brightness profiles do provide a reasonable description of the data, it is possible to derive a number of other interesting properties for these systems, such as gas mass and total mass. In fact, within the data extraction radius, the gas mass is relatively insensitive to changes in β_{fit} and core radius, as the normalisation of the gas density profile is constrained by the normalisation of the spectral fit. However, when making

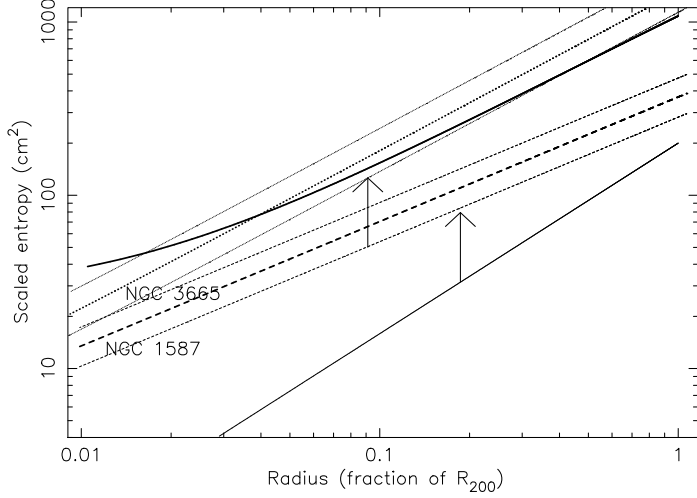


Fig. 7.— Scaled entropy (S/T) as a function of R_{200} for NGC1587 (dashed line) and NGC3665 (dotted line). The bold solid line is the average scaled entropy profile for groups as determined by Ponman et al. (2003). The fainter solid line (lower one) shows the expected canonical relationship, normalized to a 0.4 keV system (see text for details). The two arrows mark the extent of the data for the two groups in this analysis. The faint dashed and dotted lines show the approximate 1 sigma error bounds for the two profiles.

large extrapolations of the data, the masses can be quite sensitive to changes in β_{fit} and the results from large extrapolations should be viewed with some caution.

Given spectral information, together with a model for the surface brightness distribution, it is possible to derive the gas entropy in these systems. Entropy profiles were derived by assuming an isothermal temperature distribution in each, and inferring the gas density profile from a combination of the spectral data and the surface brightness profile. The entropy, defined here as $S = T/n_e^{2/3}$, where n_e is the electron density, is then readily calculated. For self-similar systems virialising at the same epoch (and hence having the same mean overdensity) one expects the entropy at a given overdensity radius to simply scale with mean system temperature (Ponman et al. 1999). Hence, for comparison between different systems, it is helpful to scale entropies by $1/T$. In Figure 7 we show such scaled entropy profiles for NGC1587 and NGC3665. Also shown for comparison is the average scaled entropy profile for a number of low temperature systems, derived by Ponman et al. (2003), and a line representing expectations from simulations involving only gravitational physics and shock heating. The latter follows the trend $S \propto r^{1.1}$ expected from analytical theories of spherical accretion of gas onto clusters (Tozzi & Norman 2001), and found in cosmological simulations. This profile has been normalised using the simulations of Voit et al. (2003), and scaled to

$T = 0.4$ keV, to match the typical temperatures of NGC 1587 and NGC 3665. This shows that both groups have entropies well above the self-similar expectations, as is typically the case in low mass systems (Ponman et al. 2003; Voit & Ponman 2003). The scaled entropy of the IGM in NGC 3665 agrees well with that seen in other poor groups, whilst that in NGC 1587 is unusually low, accounting for the location of the latter to the high side of the $L_X : T$ relation (Fig.6). It has already been pointed out by Mushotzky et al. (2003) and Sun et al. (2003) that the scaled entropy in groups shows considerable real scatter, which may reflect differences in the star-forming and merger histories within different groups.

In Table 7 we show a number of inferred parameters for our two groups, assuming spherical symmetry and an isothermal IGM. The errors on the parameters are obtained by taking the extreme effects of the errors on the spectral normalisation and temperature. For each group we show the parameters calculated at 3 different radii: the data extraction radius, $0.3R_{200}$ and R_{200} . R_{200} is calculated by deriving the over-density profile, and finding the radius which corresponds to an over-density of 200 (relative to the critical density of the Universe). For NGC 1587 this radius was 327 kpc (factor of 5 extrapolation in radius) and for NGC 3665, 409 kpc (factor of 9 extrapolation in radius).

As can be seen, these systems have fairly low total masses – the typical mass of the groups given in Mulchaey et al. (1996) is $\sim 1 \times 10^{13} M_\odot$, although those masses are derived to a variety of different radii. Our masses and group temperatures are roughly consistent with the isothermal mass-temperature relation for groups and clusters derived by Sanderson et al. (2003). The gas masses are fairly low for groups, although due to the flat gas density profiles inferred, they rise strongly with radius, as do the gas mass fractions. Despite the comparatively low gas mass and gas fractions, these values are still substantially larger than those of bright ellipticals (e.g. Bregman et al. 1992; O’Sullivan et al. 2003) at $0.3R_{200}$, and

Table 7. Group masses and related properties as determined under the assumption of an isothermal model.

	NGC 1587			NGC 3665		
	$R_{extract}$	$0.3R_{200}$	R_{200}	$R_{extract}$	$0.3R_{200}$	R_{200}
Total Mass ($h_{75}^{-1} M_\odot$)	$9.04^{+0.98}_{-0.98} \times 10^{11}$	$1.39^{+0.15}_{-0.15} \times 10^{12}$	$4.58^{+0.50}_{-0.50} \times 10^{12}$	$1.04^{+0.16}_{-0.10} \times 10^{12}$	$2.70^{+0.42}_{-0.24} \times 10^{12}$	$8.97^{+1.39}_{-0.78} \times 10^{12}$
Gas Mass ($h_{75}^{-2.5} M_\odot$)	$2.20^{+0.57}_{-0.44} \times 10^{10}$	$5.00^{+1.29}_{-1.00} \times 10^{10}$	$5.01^{+1.29}_{-1.01} \times 10^{11}$	$4.35^{+1.38}_{-0.88} \times 10^9$	$2.03^{+0.64}_{-0.41} \times 10^{10}$	$1.42^{+0.45}_{-0.29} \times 10^{11}$
Stellar Mass ($h_{75}^{-2} M_\odot$)	$\sim 2.5 \times 10^{11}$	$\sim 2.5 \times 10^{11}$	$\sim 3.1 \times 10^{11}$	$\sim 1.2 \times 10^{11}$	$\sim 1.5 \times 10^{11}$	$\sim 1.6 \times 10^{11}$
Stellar Mass Fraction (h_{75}^{-1})	~ 0.28	~ 0.18	~ 0.06	~ 0.12	~ 0.06	~ 0.02
Gas Mass Fraction ($h_{75}^{-1.5}$)	$0.024^{+0.010}_{-0.007}$	$0.036^{+0.015}_{-0.010}$	$0.109^{+0.045}_{-0.031}$	$0.0042^{+0.0019}_{-0.0013}$	$0.0075^{+0.0033}_{-0.0023}$	$0.016^{+0.007}_{-0.005}$
Baryon Fraction	~ 0.3	~ 0.22	~ 0.17	~ 0.12	~ 0.07	~ 0.04
Star formation efficiency	~ 0.92	~ 0.83	~ 0.38	~ 0.97	~ 0.88	~ 0.53
Mass-to-light ratio ($h_{75}^1 M_\odot / L_B$)	~ 22	~ 34	~ 58	~ 44	~ 89	~ 278

the values are rising more rapidly with radius in these groups, since O’Sullivan et al. (2003) find that typically $\beta_{fit} \sim 0.5$ in the halos of early-type galaxies.

In addition to the total and gas masses we also show a number of other parameters. The stellar mass is estimated by searching NED for galaxies within the appropriate radius and assuming mass-to-light ratios of $5 M_\odot/L_B$ for early type galaxies and $1 M_\odot/L_B$ for late types. Both these systems are very poor, and most of the brighter member galaxies are found in the central regions, leading to stellar mass fraction which is high in the central region, but drops off fairly rapidly with radius. The large stellar mass fraction also leads to a high mean star formation efficiency (defined as $M_*/(M_* + M_{gas})$) in the central regions. Clusters typically have efficiencies of $\sim 0.2\text{-}0.3$ (David et al. 1990; Arnaud et al. 1992), however once again these are generally derived at a much larger fraction of R_{200} than the radius to which groups are detected, and the extrapolation to R_{200} for the groups shows that there is the potential for a substantial drop with radius.

The baryon fractions and mass-to-light ratios are both roughly consistent with the range of values seen in Mulchaey et al. (1996). The baryon fraction shows less radial variation than most of the other parameters, as the effect of the rising gas mass fraction and dropping stellar mass fraction partially cancel out to produce a flatter baryon fraction profile. The baryon fraction of NGC 1587 is roughly consistent with the typical values of 0.1-0.3 seen in clusters (e.g. David et al. 1995; Hradecky et al. 2000), while NGC 3665 is a little lower than this.

Thus overall these two systems have properties which appear to be broadly consistent the scaling relations observed in other galaxy systems (apart from the $L : \sigma$ relation as discussed below). In the few cases where there may be some significant differences (e.g. star formation efficiency) these two groups tend to differ in the sense that they appear more like individual galaxies, although some care is needed as some of these properties have the potential for significant radial changes. For example, the star formation efficiency is clearly dropping with radius, and at values close to R_{200} this value could be consistent with clusters given the uncertainties involved in the extrapolation.

We conclude that in most respects, NGC 1587 and NGC 3665 appear to be fairly normal, low mass, groups. Given this, there is no reason to expect them to have a significant offset from the group $L : \sigma$ relation. However as discussed in the introduction, these two groups are significantly offset from an extrapolation of the cluster $L : \sigma$ relation, and this offset is in a direction opposite to what would be expected, given the effects of preheating. If the X-ray luminosities really are comparatively normal, especially in the case of NGC 3665, then perhaps the velocity dispersions are unusual in some way.

As mentioned earlier in §2, the original velocity dispersions of these systems were esti-

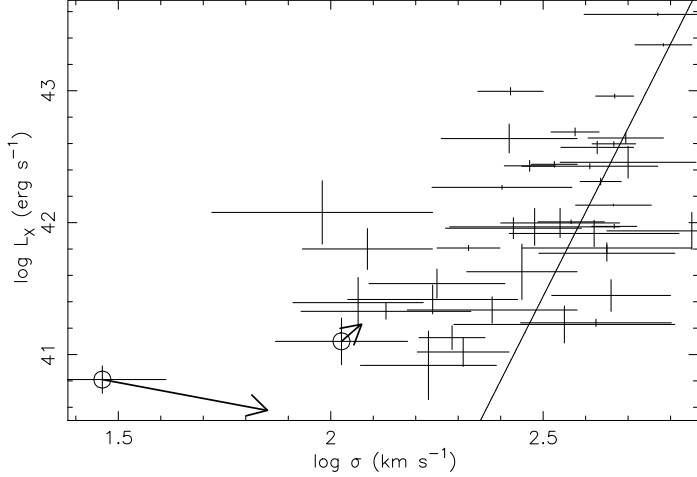


Fig. 8.— The $L_X : \sigma$ relation using data from Helsdon & Ponman (2000b) with arrows showing how NGC 1587 and NGC 3665 have moved as a result of the analysis in this paper. The line marks the cluster line as derived by White et al. (1997).

mated from very few galaxies, which suggests that they may be suspect. However, as shown above, the addition of related galaxies from NED was able to significantly increase the group membership, and confirm the low velocity dispersions. One can attempt to further refine these dispersions by only including galaxies within the virial radius in projection (1 Mpc was used earlier). This has the effect of dropping the membership to 6 galaxies for both groups, leading to a velocity dispersion of 101 ± 29 for NGC 1587 and 61 ± 17 for NGC 3665 – values which are actually almost identical to those obtained under the less strict membership requirements used in §2.

The measured velocity dispersion for NGC 3665 is immediately suspect, as a virialised system must have a minimum mean density related to the density of the universe, which can be used to constrain the velocity dispersion of a virialised group to be at least $100-200$ km s^{-1} (Mamon 1994). The velocity dispersion of NGC 3665 is clearly below this limit and the dispersion of NGC 1587 is also uncomfortably low. Even after correcting for statistical biases in the group velocity dispersion (the standard method of calculating velocity dispersions is biased low, and this bias is most significant when the number of group members is low – Helsdon & Ponman in prep.) these velocities are only increased to 117 km s^{-1} and 70 km s^{-1} respectively. Figure 8 shows how NGC 1587 and NGC 3665 move on the group $L : \sigma$ relation if these velocity dispersions are used along with the Chandra luminosities derived earlier. The other data points in Figure 8 are taken from Helsdon & Ponman (2000b).

Since we have mass profiles from our X-ray analysis, we can predict the velocity dispersion we would expect to see within the group, under given assumptions about the galaxy orbits. In the simple case of an isothermal sphere, with isotropic velocities, $\sigma^2(r) = GM(r)/2r$, and using the masses given in Table 7, we obtain a predicted velocity dispersion for NGC 1587 of ~ 174 km s $^{-1}$, and for NGC 3665 of ~ 217 km s $^{-1}$ (these predictions are essentially the same for each of the three mass/radius combinations in the table) – both much larger than the measured values. Lokas & Mamon (2001) calculated the line-of-sight velocity dispersions which would be observed for galaxies orbiting within halos with density profiles which follow the “NFW” profile of Navarro et al. (1995), for a range of halo concentration parameters and orbital anisotropies. In general, these results show that the isothermal sphere assumption gives a reasonable approximation to the integrated value of σ for likely halo concentrations. Purely radial orbits result in $\sigma(r)$ profiles which rise sharply in the centre, whilst circular orbits result in a central minimum in $\sigma(r)$. However, for velocity dispersions calculated (as here) for galaxies falling within R_{200} , all reasonable models produce mean velocity dispersions which fall within $\sim 20\%$ of the isothermal value.

If the velocity dispersion values predicted from the masses above are a fair estimate of the ‘real’ velocity dispersion, then some process must have reduced the velocity dispersion of the galaxies in these systems. One possible candidate is dynamical friction. The timescale for dynamical friction in these two groups can be estimated using the equations given by Binney & Tremaine (1987) which integrate the Chandrasekhar (1943) dynamical friction force as a galaxy falls towards the group centre. We assume that the total gravitational mass is proportional to r^{-2} , and that a galaxy is initially on a circular orbit at a radius of 200 kpc (a little below the predicted virial radius for NGC 3665, and approximately the average radius of galaxies in NGC 1587) with a velocity of $\sqrt{2}\sigma_p$, where σ_p is the predicted velocity dispersions for the group as described above. Under these assumptions an L_* galaxy with a typical mass to light ratio of $10 M_\odot/L_\odot$ is predicted to fall to the group center in ~ 2.9 Gyr for NGC 1587 and ~ 3.9 Gyr for NGC 3665. Thus the effects of dynamical friction acting over a substantial fraction of the Hubble time could be significant in both these groups.

Dynamical friction leads to a transfer of energy from a large orbiting body, to the sea of dark matter particles through which it moves. Another possibility is that orbital energy may be converted into internal energy of galaxies, via tidal interactions. This effect is not significant in clusters, since the orbital velocities of galaxies are substantially higher than their internal velocity dispersions. In the present case, however, the reverse is true, and strong tidal encounters between the slowly moving galaxies could absorb substantial orbital energy, leading to circularisation and lowering of orbits. Both effects would reduce measured line-of-sight (los) velocity dispersions to some extent.

A third possibility, is that in NGC1587 and NGC3665, much of the orbital motion happens to take place in the plane of the sky, and does not contribute to the line of sight velocity dispersion. Since groups generally form within cosmic filaments, in cosmological simulations, it would not be surprising to find significant elongation and an anisotropic velocity dispersion tensor in many systems (e.g. Tovmassian et al. 2002). Distributing such systems at a variety of angles to the los, will then result in additional scatter (over and above that expected from random sampling of an isotropic velocity distribution) in σ . Such non-statistical scatter is certainly observed in the $\sigma : T$ relation (Helsdon & Ponman 2000b). In this picture, low σ groups have 3-dimensional velocity dispersions which are substantially more than $\sqrt{3}\sigma_{los}$, and there will be other groups for which the reverse is true.

5. Acknowledgments

The authors would like to thank Ben Maughan for helpful discussions on the Cash statistic and for assistance with the Cash statistic simulations. We would also like to thank Gary Mamon for helpful discussion of the velocity dispersion in groups. Partial support for this project was provided by SAO grants GO1-2134X and AR3-4013X.

REFERENCES

Arnaud, M., Rothenflug, R., Boulade, O., Vigroux, L., & Vangioni-Flam, E. 1992, A&A, 254, 49

Bartelmann, M. & Steinmetz, M. 1996, MNRAS, 283, 431

Binney, J. & Tremaine, S. 1987, Galactic Dynamics (Princeton University Press, Princeton, New Jersey)

Bower, R. G. 1997, MNRAS, 288, 355

Bregman, J. N., Hogg, D. E., & Roberts, M. S. 1992, ApJ, 387, 484

Cash, W. 1979, ApJ, 228, 939

Chandrasekhar, S. 1943, ApJ, 97, 255

David, L. P., Arnaud, K. A., Jones, C., & Forman, W. 1990, ApJ, 356, 32

David, L. P., Jones, C., & Forman, W. 1995, ApJ, 445, 578

Dickey, J. M. & Lockman, F. J. 1990, *ARA&A*, 28, 215

Freeman, P. E., Doe, S., & Siemiginowska, A. 2001, in SPIE Proceedings, Vol. 4477, 76

Helsdon, S. F. & Ponman, T. J. 2000a, *MNRAS*, 315, 356

—. 2000b, *MNRAS*, 319, 933

Hradecky, V., Jones, C., Donnelly, R. H., Djorgovski, S. G., Gal, R. R., & Odewahn, S. C. 2000, *ApJ*, 543, 521

Lokas, E. L. & Mamon, G. A. 2001, *MNRAS*, 321, 155

Mahdavi, A., Böhringer, H., Geller, M. J., & Ramella, M. 2000, *ApJ*, 534, 114

Mahdavi, A. & Geller, M. J. 2001, *ApJ*, 554, L129

Mamon, G. A. 1994, in Clusters of Galaxies, ed. F. Durret, A. Mazure, & J. Tran Thanh Van (Frontieres: Gif-sur-Yvette), 291

Mulchaey, J. S., Davis, D. S., Mushotzky, R. F., & Burstein, D. 1996, *ApJ*, 456, 80

—. 2003, *ApJS*, 145, 39

Mulchaey, J. S. & Zabludoff, A. I. 1998, *ApJ*, 496, 73

Mushotzky, R., Figueroa-Feliciano, E., Loewenstein, M., & Snowden, S. L. 2003, *astro-ph/0302267*

Navarro, J. F., Frenk, C. S., & White, S. D. M. 1995, *MNRAS*, 275, 720

Osmond, J. P. F. & Ponman, T. J. 2003, *MNRAS*, submitted

O'Sullivan, E., Forbes, D. A., & Ponman, T. J. 2001, *MNRAS*, 328, 461

O'Sullivan, E., Ponman, T. J., & Collins, R. S. 2003, *MNRAS*, 340, 1375

Ponman, T. J., Bourner, P. D. J., Ebeling, H., & Böhringer, H. 1996, *MNRAS*, 283, 690

Ponman, T. J., Cannon, D. B., & Navarro, J. F. 1999, *Nature*, 397, 135

Ponman, T. J., Sanderson, A. J. R., & Finoguenov, A. 2003, *MNRAS*, 343, 331

Pratt, G. W. & Arnaud, M. 2003, *A&A*, 408, 1

Rasmussen, X. X. & Ponman, T. J. 2003, *MNRAS*, submitted

Sanderson, A. J. R., Ponman, T. J., Finoguenov, A., Lloyd-Davies, E. J., & Markevitch, M. 2003, MNRAS, 340, 989

Sun, M., Forman, W., Vikhlinin, A., Hornstrup, A., Jones, C., & Murray, S. S. 2003, ApJ, accepted, astro

Tovmassian, H. M., Yam, O., & Tiersch, H. 2002, ApJ, 567, L33

Tozzi, P. & Norman, C. 2001, ApJ, 546, 63

Voit, G. M., Bryan, G. L., Balogh, M. L., & Bower, R. G. 2002, ApJ, 576, 601

Voit, G. M., Kay, S. T., & Bryan, G. L. 2003, in prep

Voit, G. M. & Ponman, T. J. 2003, ApJ, 594, L75

White, D. A., Jones, C., & Forman, W. 1997, MNRAS, 292, 419

Wu, X., Xue, Y., & Fang, L. 1999, ApJ, 524, 22